Progress In Electromagnetics Research B, Vol. 57, 21–46, 2014

Fully Time-domain Scanning of EM Near-Field Radiated by RF Circuits

Yang Liu and Blaise Ravelo*

Abstract—This paper deals with planar scanning technique of electromagnetic (EM) near-field (NF) emitted by electronic printed circuit boards (PCBs) fully in the time-domain (TD). The proposed EM scanning metrology is essentially based on the NF test bench available at the IRSEEM laboratory. It comprises motorized mechanical structures for moving the probe interconnected to electronic measurement instruments and controlled by a driver PC. The synoptic of the test bench is presented and technically examined. The characteristics of different elements constituting the measurement chain of the TD test bench understudy are described. The NF metrology developed is originally focused on the measurement of time-dependent magnetic field $H(t)$ dedicated to the radiated emission electromagnetic compatibility (EMC) applications. An innovative calibration technique of the loop probe for detecting $H(t)$ is established in order to ensure the post processing and extraction of the measured NF data. Then, validations were carried out via comparison with different simulations run with standard commercial tools. Mathematical analyses were also conducted for the improvement of the measurement post processing. To realize the mapping of time-dependent EM field components, a software interface edited with the graphical language LabVIEW was emulated to synchronize the probe displacement and the data acquisition. An UWB amplifier with average gain about 30 dB from DC to 300 MHz was designed and fabricated in order to decrease the measurement noise and to improve the quality of measured signals. As results of the study, TD NF mapping is demonstrated successfully by measuring the EM radiation emitted by electronic planar circuits. The technique developed is extremely useful in the field of EMC engineering for predicting the transient perturbations susceptible to degrade electronic functions in complex systems encountered usually for the automotive and aeronautic applications.

1. INTRODUCTION

With the increase of electromagnetic (EM) pollution, the radio communicating devices can be affected by noisy transient signals occurred as unwanted electrical interferences [1–3]. Owing to these undesired EM effects, an estimation method was proposed in [4] for analysis of an effect related to the printed circuit board (PCB) radiation. According to the EM compatibility (EMC) compliances related to the EM level radiation [5, 6], standard techniques were proposed in the literature. Due to the high density of integration, the EM near-field (NF) coupling between the neighboring components in the limited space becomes critical for the system safety. To cope with this harmful coupling, characterization methods for microelectronic [7] and power electronic [8] circuits were proposed.

With the increase of complexity, the EMC modeling becomes a crucial step for the analysis of electronic devices in different areas as automotive [9–11] and aircraft [12–14] systems. For this reason, time-domain (TD) characterization techniques [15] and hybrid modeling approaches [16] for the EMC measurements were put forward recently. Nevertheless, in the area of EMC engineering, the NF emission remains one of the cumbersome shortcomings to be stuffed with the complexity of PCBs. Owing to this daunting problem, NF characterization methods enabling to predict the radiation of electronic

Received 29 July 2013, Accepted 11 October 2013, Scheduled 21 November 2013

* Corresponding author: Blaise Ravelo (blaise.ravelo@yahoo.fr).

The authors are with the IRSEEM, EA 4353 at the Graduate School of Engineering ESIGELEC, Technopole du Madrillet, Av. Galilée, BP 10024, St Etienne du Rouvray Cedex F-76801, France.

circuits as microcontroller and PCBs were introduced in [17–25]. Emphatically, the analytical model developed in [22–25] is usually based on the inverse method from the maps of EM field emitted by the tested circuits. More precisely, this inverse method consisted in synthesizing the amplitude of the excitation and geometrical orientation of elementary dipole arrays placed virtually in the surface or metallic plane of the emitting circuit. This method was at the beginning established in the frequency domain (FD). But in certain cases of transient perturbation, only the FD analysis is insufficient. TD investigation [26–29] needs to be developed according to the targeted applications. Then, thanks to the 2D data time-frequency transposition computation introduced in [30], the NF model with equivalent dipole arrays was extended into the TD [31]. Based on the plane wave spectrum (PWS) theory, further TD NF processing as extraction of EM field longitudinal component from transversal components [32, 33] and NF/NF transform [34] was settled. In addition, TD modeling approaches based on recursive full wave computation methods (FDTD, TD-FEM, TD FE–boundary integral method...) [35–40] were also democratized and exploited for predicting the transient radiation of geometrically reproducible simple structures. With such computational EM methods (CEMs), validation methods of electronic structure NF emission were suggested [41, 42]. More popularly, advanced simulation tools (ADS, ANSYS, CST, FEKO, EMC studio, Quickwave 3D...) integrating more and more solvers (frequency and transient solver, TLM solver, MoM solver...) were released and currently commercially available [43–48].

It is worth noting that when the PCBs comprise complex and high density integrated circuits, no simulation tool can be used for computing the NF emissions. For this reason, NF measurements are technically judged as an essential way in particular for complex circuits. Different techniques of NF measurements [4, 7, 8, 12–17, 48–57] have been established. Among the existing techniques, the direct measurement with NF scan developed in IRSEEM [48–51, 54] based on the electronic probes constitutes one of the best trade offs in term of simplicity, accuracy, measurement time duration and test cost. The functioning principle of the IRSEEM NF test bench is illustrated by Fig. 1.

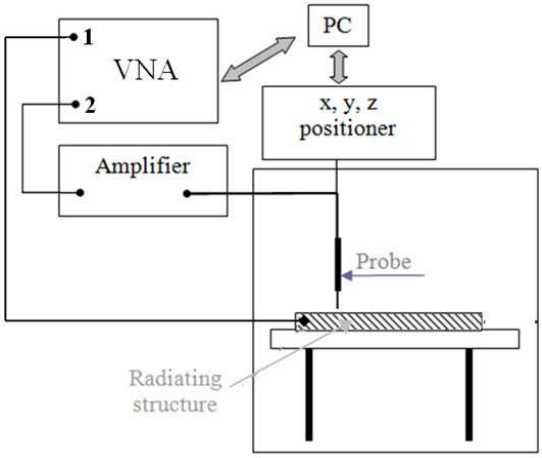

Figure 1. Synoptic diagram of the experimental setup with the IRSEEM NF test bench [48–51].

One can point out that the test bench global block diagram is comprised of:

- ☐ A probing system dedicated to convert the detected EM NF into electrical parameters as voltage and current;
- ☐ The measurement instruments to record the data as vector network or spectrum analyzer (VNA/SA) and to provide the DUT excitation as the signal generator;
- ☐ A displacement system essentially consisted of a robotic arm is necessary to hold, to place and to move the probe in the targeted surface scan;
- ☐ A personal computer (PC) is used to record the measured data from the instrument and to control the movement of the robot.

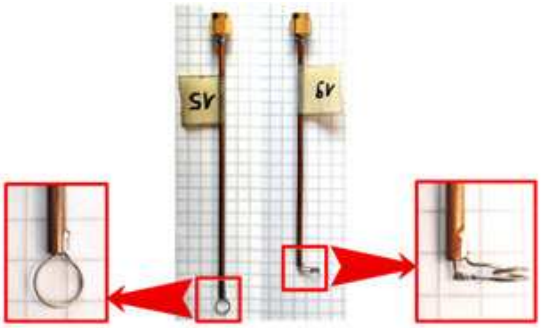

Figure 2. Photographs of loop probes used for the magnetic NF measurement.

However, till now, the majority of this type of NF RF metrology is implemented only in the FD, such as the NF test bench developed in IRSEEM [48–51]. This test bench is dedicated to the scanning of EM NF radiated by electrical or electronic components or systems in the frequency range from some hundred Hz to some GHz. Facing the ultra-short transient emission generated during the high-speed current or voltage switching, for example in the digital system, the FD scanning is no longer enough for investigating the transient NF radiation. For this reason, the main object of this paper is the development of TD NF test bench with direct scan technique. To do this, we will regenerate the cartographies of time-dependent EM NF radiated by the electronic circuits under test as described in the following sections.

2. RECALL ON THE ELECTRONIC PROBES NF SCANNING CALIBRATION IN THE FD

It is worth noting that the electronic probes used to perform this NF scan are none other than small sensors or antennas as proposed in [48–51]. These sensors are fixed and moved in the surface test plane localized in the near-zone above the radiating device as seen in Fig. 1. Knowing the antenna factor (AF), we determine the detected NF with the following mathematical equation from the voltage provided by the probes:

$$E, H\,(f) = AF^{-1}\left[v, i\,(f)\right], \tag{1}$$

Suitable probes need to be employed to scan the electric or magnetic NF components (X_x, X_y, X_z) according to the position of the DUT in the considered system reference *Oxyz*. For example, to detect the electric NF components, electric dipole and monopole probes can be used whereas the scan of magnetic NFs requires in turn loop probes as exposed in Fig. 2. To record the frequency data corresponding to the EM NF radiated by the structure delivered by these probes, VNA or SA are used. The probe is moved in the targeted scanning surface via a manual or automated mechanical system in order to generate the EM NF cartography. As depicted in Fig. 2, probes having two different orientations of metallic loops are used to measure the magnetic NF horizontal and vertical components. The probe presented on the left is dedicated to the magnetic field horizontal components H_x and H_y, and the other is used for the vertical component H_z. As visualized in Fig. 3, two NF test benches with the same functioning principles are available at IRSEEM. Their technical difference lies in the physical size of the DUT and the spatial resolution of the scanning surface. The bigger one presents a physical size with geometrical surface of about $1\,\text{m} \times 2\,\text{m}$. Its minimal spatial resolution or the smallest step of the displacement robot system is equal to $10\,\mu\text{m}$. The smaller one is devoted to the electronic or electric circuits with a maximum about $50 \times 50\,\text{cm}^2$. Its best spatial resolution is $5\,\mu\text{m}$ or two times higher.

Since the measurement principle employed in the TD is quite similar to that performed in the FD, the employed electronic probes can also be used for the TD measurement as a function of the considered operating frequency bandwidth. Due to the difficulty on the calibration and fabrication of electric field probes appropriated to the targeted applications, this work is focused on the magnetic NF emission measurements in the TD.

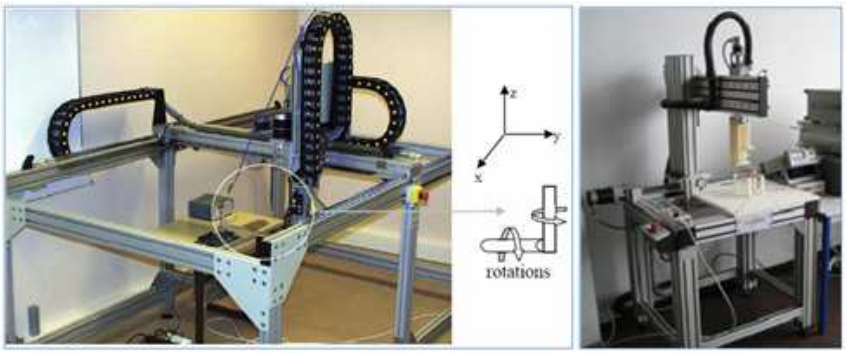

(a) (b)

Figure 3. Photographs of IRSEEM NF test bench for (a) electronic systems and (b) components.

3. DEVELOPMENT OF THE TD NF SCANNING MEASUREMENT TEST BENCH

Through the present work, our purpose is to develop a full TD test bench by providing time-dependent NF cartography of planar electronic circuits. With description of the test bench synoptic, the algorithmic process of the interface to the mechanical control allowing the scan procedure and synchronized with the signal acquisitions is thoroughly inspected.

3.1. Description of the TD NF Measurement Synoptic

From a general point of view, the main difference between the proposed TD test bench and the existing frequency one is the replacement of the measured data receiver VNA/SA by digital oscilloscope. Obviously, the induced time-dependent voltage $v(t)$ corresponds analytically to $H(t)$ radiated by the DUT. Then, by establishing the TD transfer function of the loop probe used, one can deduce the transient magnetic field $H(t)$ from $v(t)$ via the calibration equation $H(t) = f[v(t)]$. Then, the TD NF mapping is restituted by scanning in the measurement plane and the treatment of the voltage delivered by the scope. The displacement of the probe fixed at the extremity of the arm of a mechanical robot is programmed with the PC equipped by command software described later in the next subsection. For the further understanding, the block diagram illustrating the TD NF test bench is described in Fig. 4. With this test bench, the path of the data flow can be also observed. As stressed in Fig. 4, the test bench is composed of the excitation source, H-field probe, digital oscilloscope, displacement robot, and PC which stores the data delivered by the oscilloscope and controls the robot displacement. It is worth noting that two RF amplifiers are used in this test bench. They may be required by virtue of the level of the signals from the probes. The power amplifier is used to amplify the excitation signal, in order to generate a significant level of EM radiation with the circuit under test. It is obvious that the stronger excitation might make the circuit radiate intensely; the better voltage signal would be recorded by the oscilloscope. It could be quite helpful, when we need to assess the H-field emitted by passive circuit. The UWB amplifier placed between the probe and the oscilloscope is necessary to amplify the voltage signal induced by the radiated field. The performance of the TD test bench depends mainly on the employed digital oscilloscope which constitutes one of the key equipments of the entire test chain. During the test, the digital oscilloscopes MSO6104A or DSO6034A from Agilent^{TM} available at IRSEEM, whose the main technical specifications are addressed in Table 1, have been used.

We can remark that MSO6104A is more powerful than DSO6034A. However, they have the same memory depth and display a resolution which can provide the saved waveform with 1000 points in the file exported. The digital oscilloscope is connected to the PC via GPIB cable. Then, the PC achieves the data acquisition via a specific software interface emulated in LabVIEW graphical language provided by NI^{TM}.

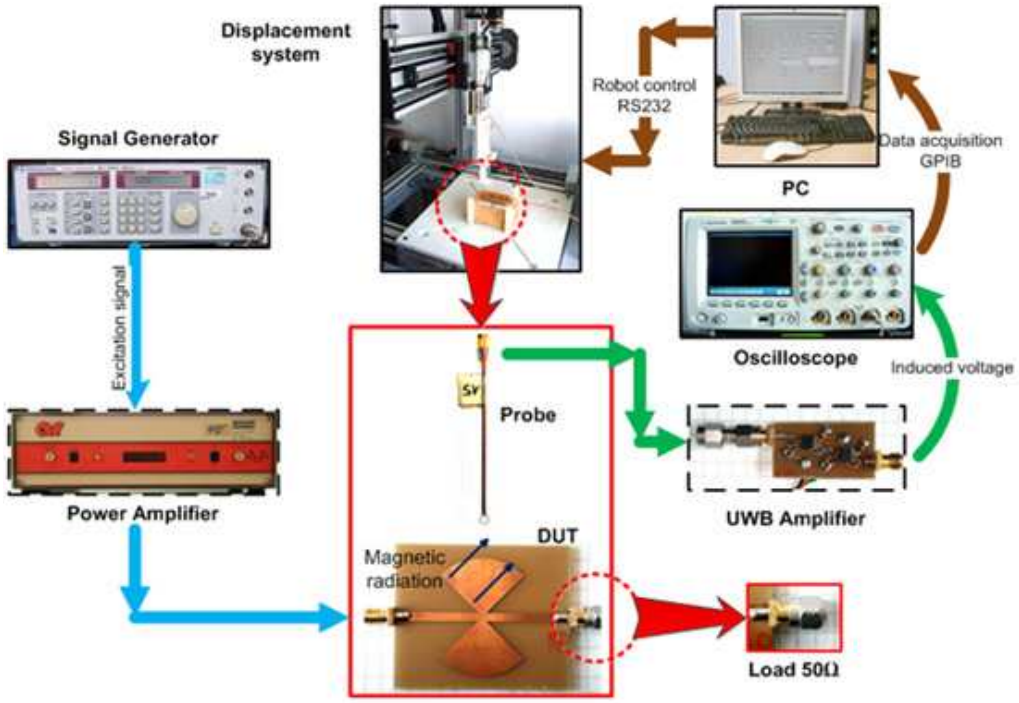

Figure 4. Synoptic of the TD NF measurement system understudy.

Table 1. Technical specifications of the used oscilloscopes (Agilent- MSO6104A and DSO6034A).

Technical specifications	Agilent MSO6104A	Agilent DSO6034A
Bandwidth	1 GHz	300 MHz
Sample Rate	4 GSa/s	2 GSa/s
Max Memory Depth	8 Mpts	
Channels	4 analog + 16 digital	4 analog
Vertical Range	2 mV/div to 5 V/div, ±40 V	
Horizontal Range	500 ps/div to 50 s/div	2 ns/div to 50 s/div
Display resolution	640 vertical by 1000 horizontal points (waveform)	

3.2. Emulation of the Driver Interface for Controlling the TD Test-bench

To control the displacement robot and acquire the measurement data, a software interface is obviously necessary. The interface requires a driver program adapted to GPIB port for the data acquisition and RS-232 serial com port for controlling the robot. This driving module edited in LabVIEW was developed. We choose this language due to its flexibility for the graphical program interface and also its adaptability to the various applications for the instrument control. In the present contact, the instruments to be controlled are Agilent digital oscilloscopes connected to the PC via the GPIB port and the stepper motors of the robot of the test bench, which are manufactured by RHONAX, via the serial com port. The interface TDNF (Time-Domain Near-Field) shown in Fig. 5 was emulated especially for the data acquisition and storage and also the robot control. With this measurement interface, all the functions below can be guaranteed:

- ☐ To define the reference point of the origin of the coordinate system;
- ☐ To display the current position of the robot and measurement progress;
- ☐ To move the arm of the robot;

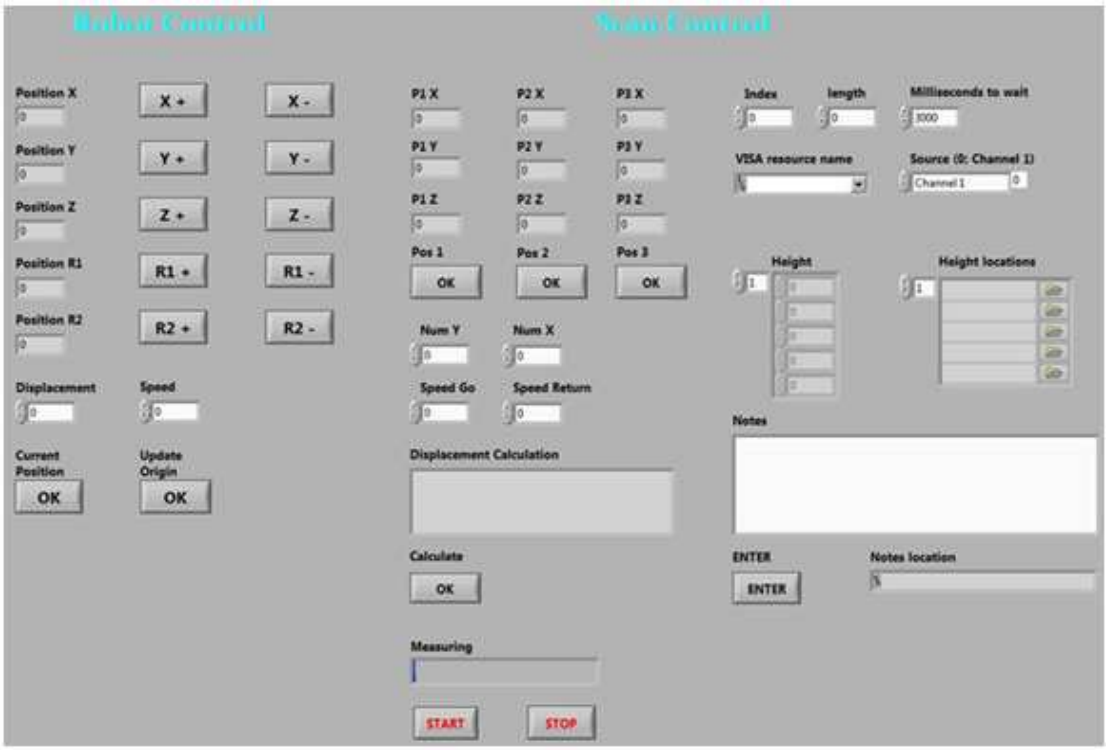

Figure 5. TDNF software interface for the TD test bench control.

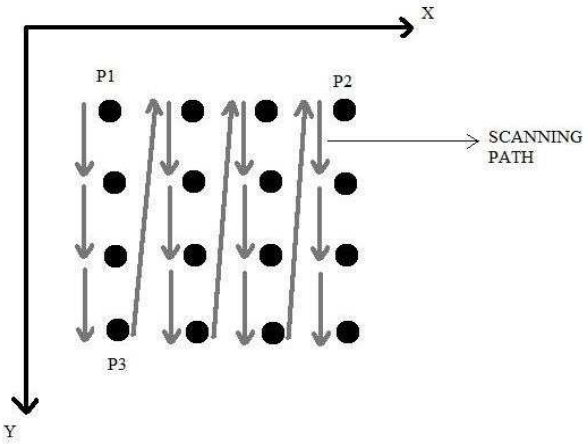

Figure 6. Diagram showing the path taken by the robot during a scan in the surface defined by (P_1, P_2, P_3).

- ☐ To define the displacement speed and spatial step;
- ☐ To define the scan surface, scan automatically in different surfaces;
- ☐ To choose the parameters of the oscilloscope;
- ☐ To calculate the distance of step and note the scan information;
- ☐ And to save the NF scanned data file generally in format $*$.txt.

The edited program is integrated with the LabVIEW Runtime library, so it can be run without installing the LabVIEW software. It means that this interface can be used with any PC without modification of the source code. The program was written such that the probe is placed at the scanning surface point.

The scan process takes place in a column-wise fashion, i.e., scanning towards the y-axis and moving on to the next column in the x-axis, as explained in Fig. 6. In the first step, it records the measured data, and then, it moves on to the next point and repeating the same process until the ending point of the surface scan defined by the triplet (P_1, P_2, P_3). After the scan of the pre-defined surface, the probe returns back to the origin point P_1. If more surfaces are to be scanned at different heights, the probe then moves up by the number of steps specified in the height field.

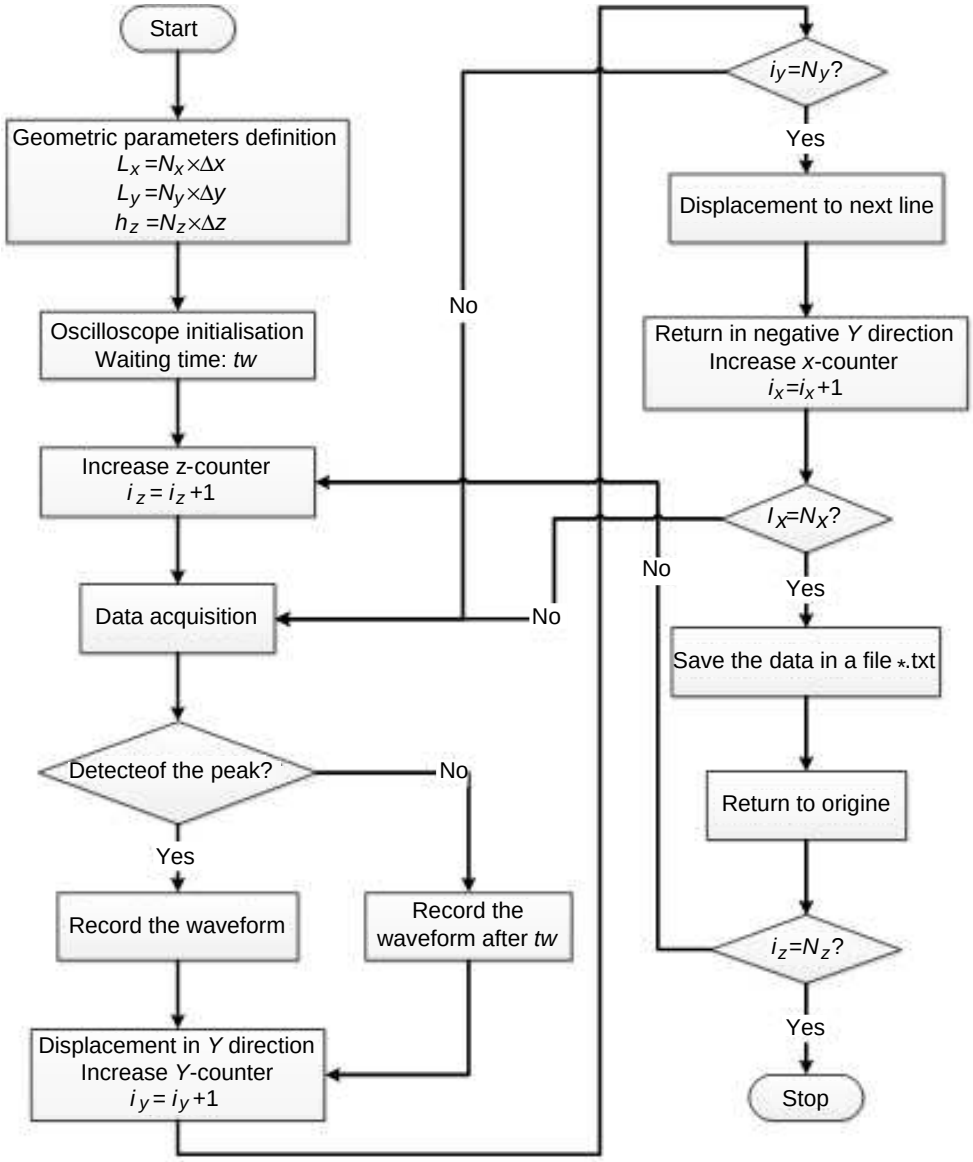

Figure 7. Work flow illustrating the algorithm executed with the TDNF software interface.

The test bench work flow algorithm is illustrated in Fig. 7, which is followed and executed via the TDNF interface to realize the function of the data acquisition and the displacement control.

4. TD CALIBRATION OF THE METALLIC PROBE USED DURING THE TEST

Because the EM probes are assumed as an indirect sensor, the radiated NF induces a voltage which is assumed as an intermediate quantity measured with the oscilloscope. To deduce the radiated NF from the induced voltage, an adequate mathematical relation to extract the right value of the field is

obviously necessary. For this purpose, a calibration technique of the probe is required to establish the analytical relation between induced voltage and the radiating field in the TD. To verify the efficacy of the transfer function, different methods are considered.

4.1. Analytical Investigation on the $H(t)$ Extraction from the Measured Data

The 3D design of the magnetic field probe is visualized in Fig. 8. It is clear that only the magnetic field normal component acts to the delivered voltage. By denoting $H(t)$ the magnetic field and $v(t)$ the induced voltage between the output terminals of the loop, according to Faraday's law, we have:

$$v\left(t\right) = -d\Phi\left(t\right)/dt = -\partial \iint_{S} B\left(t\right) dS/\partial t, \tag{2}$$

where $\Phi(t)$ is the magnetic flux through the loop's surface. Then, knowing the surface S, one can obtain the following formula where $B(t)$ is the magnetic flux density and $S = \pi r^2$ with r the radius of the loop. Finally, we can obtain the mathematical relation between $v(t)$ and $H(t)$, expressed as:

$$H\left(t\right) = -\left[\int v\left(t\right) dt\right] \Big/ \left(\mu_0 \pi r^2\right). \tag{3}$$

To confirm the relevance of this theoretical principle, TD H-field analysis was performed based on the use of 3D EM simulation with Maxwell3D. Fig. 9 represents the 3D design of the whole structure understudy including the magnetic probe. It is constituted by a circular loop of cylindrical cooper having 6 mm diameter.

The inner diameter of the loop is equal to 2.6 mm. As tinted in Fig. 9, the revolution axis of this probe indicates the direction of the NF component to be measured. On the present position, we measure the component H_y. As a function of magnetic field intensity, flowing in the spire, this probe induces a transient voltage here denoted V_{out} through its output arms.

As understood in Fig. 9, the structure understudy is composed of a magnetic probe positioned at $h = 2$ mm above the metallic plane of the Chebychev filter which is assimilated as the DUT. Then, we compared the magnetic NF from Maxwell3D simulations and Matlab calculations. In the next step, the DUT was excited by a realistic sample of periodical pulse current (with arbitrarily chosen parameters $t_{\max} = 25$ ns and $\Delta t = 2.5$ ns) plotted in top of Fig. 10. On one hand, this excitation signal was injected to the simulated structure and exhibiting then the field $H_{sim}(t)$. On the other hand, we measured the voltage $V_{out}(t)$ delivered by the probe, and the result is plotted in the bottom of Fig. 10. Thus, toward Formula (3), the radiated field $H_y(t)$ displayed in Fig. 11 was calculated. This figure represents the comparison between $H_y(t)$, directly generated from simulated and extracted with Matlab calculations which are lines respectively in red and blue. So, a slight difference between the amplitudes of simulated and calculated fields is observed. This difference is obviously due to the probe imperfections as the influence of the wire thickness which is about 0.5 mm and the non-uniformity of H_y in the surface loop.

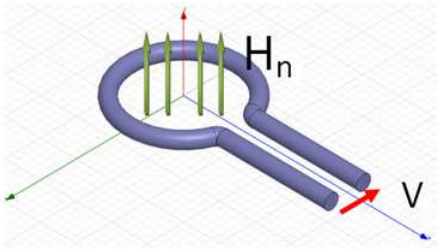

Figure 8. EM interactive illustration and 3D design of magnetic field probe.

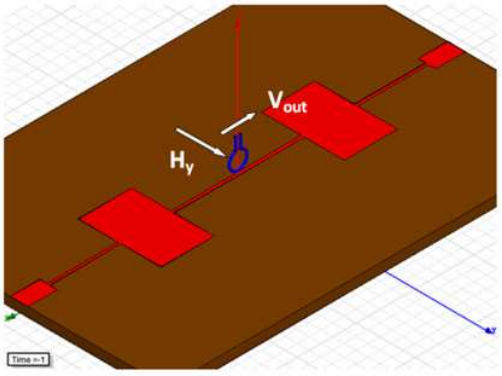

Figure 9. Maxwell 3D design of the structure understudy including the electronic probe.

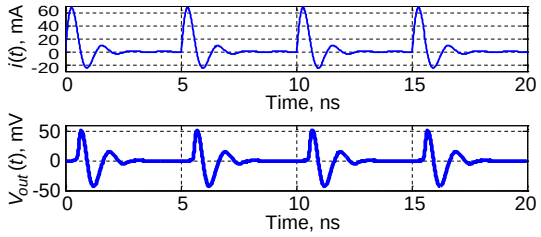

Figure 10. Transient excitation current and output of the probe employed in Fig. 9.

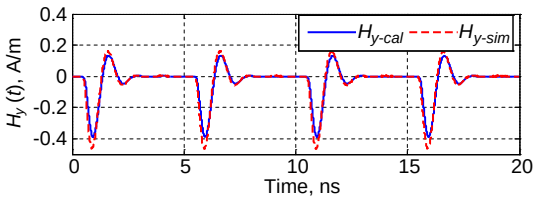

Figure 11. Comparison between $H_y(t)$ at the center of the probe shown in Fig. 9. obtained by full wave simulation and Matlab calculation.

The probe wire thickness can create a considerable difference between the loop inner and outer radius. Also, the opening and terminal arms of the loop here in the order of mm are not taken into account for the field extraction. A feasibility analysis is done by considering complex signals in order to provide the TD measurement approach. One emphasizes that offset errors appear in high and low steady states of the time-dependent magnetic field. This deviation is generally due to the numerical calculation accuracies which are linked to the number of sampling points under consideration. Afterward, the transfer function of the magnetic field probe is extracted via 3D EM simulations with different types of excitation signals. In the next step of this study, the probe will be calibrated according to its transfer function by considering different methods.

4.2. Calibration of the Magnetic Probe with Simulation Tools through Circuit Models

In order to improve the sensibility of the TD NF measurement chain, we insert an UWB amplifier between the probe and the measurement instruments as sketched earlier in Fig. 1. To determine correctly the field value from the measured voltage, the calibration of the full measurement chain is necessary. This calibration can be performed directly by simulations. The simulation tools used to implement the calibration of the measurement chain can be divided into two different categories: in circuit configuration and in full wave with 3D design. To proceed with circuit configuration, we use the electronic/microwave circuit simulator Advanced Design System (ADS) from Agilent^{TM}. This CAD tool is known as a standard tool for the RF/microwave circuit design and simulation. To perform the full wave analysis, we use different tools, such as HFSS and Maxwell3D from Ansys^{TM} and Computer Simulation Technology Microwave Studio (CST MWS) whose basic characteristics are summed up in Table 2.

Table 2. Characteristics of simulation tools considered for 3D EM full wave simulation.

Simulation software	Solver method	Simulation domain	Frequency Band
HFSS	Finite Element Method (FEM)	Frequency	High frequency
Maxwell 3D		Frequency & Time	Low frequency
CST Microwave Studio	Finite Integration Technique (FIT)	Frequency & Time	From DC to high frequency

4.2.1. Theoretic Model of the Loop Probe

The magnetic field probe is considered as a magnetic loop antenna with a non-constant AF versus frequency. Indeed, the loop antenna can be electrically modeled as the LC circuit depicted in Fig. 12. L is the loop inductance with its resistance R_i, C the capacitance, R the load resistance (assumed to be independent of the frequency), and V_{mes} the voltage across the load resistance which is related to the magnetic field. The inductance of a single-turn loop is given by [59]:

$$L = \mu_0 b \left[\ln\left(8b/a\right) - 2\right], \tag{4}$$

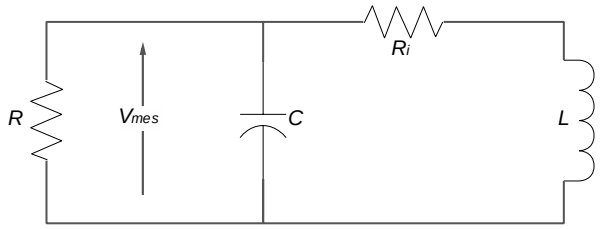

Figure 12. Equivalent circuit model of the considered loop probe.

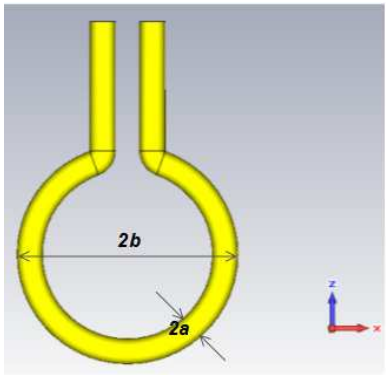

Figure 13. Geometric parameters of the loop.

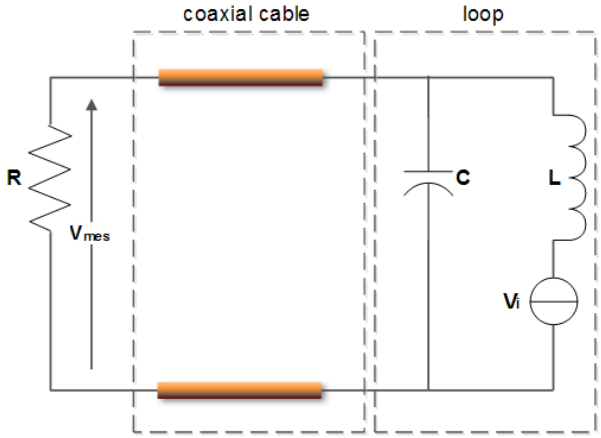

Figure 14. Circuit model of the full measurement chain of the loop and its metallic arm.

where b and a are the loop and wire radii as highlighted in Fig. 13. The capacitance of the loop is given by [59]:

$$C = 2\varepsilon_0 b/\left[\ln\left(8b/a\right) - 2\right], \tag{5}$$

By denoting σ the conductivity of the loop conductor, we can define the resistance R_i with the formula [59]:

$$R_i = b/a\sqrt{\omega\mu_0/(2\sigma)}, \tag{6}$$

As we can see, R_i is dependent on the radian frequency $\omega = 2\pi f$. In practice, this resistance can be neglected. So, the circuit model of the magnetic loop is simplified. Afterwards, by introducing the induced voltage from the magnetic field $H(t)$ as a voltage source V_i, we build the circuit model of the full measurement chain described in Fig. 14. This circuit model was explored to determine the relation between V_{mes} and V_i in order to improve the accuracy of experimented data. To verify the effectiveness of this calibration technique with circuit configuration, a demonstration is performed with the simulation tools.

4.2.2. Validation Results of the Probe Calibration

To spawn the circuit model, the parameters' values of the probe pictured in left of Fig. 2 were calculated with Equations (4) and (5) with physical characteristics addressed in Table 3. Then, the circuit model including the coaxial cable model was implemented in ADS as in Fig. 15. Moreover, a 3D model of the probe was designed with CST MWS. So, the magnetic probe is considered as a single port passive

Table 3. Physical characteristics of the magnetic probe in left of Fig. 2.

Loop radius	3 mm
Wire radius	255 µm
Radius of the outer conductor of coaxial cable	0.84 mm
Wire metal	copper
Dielectric permittivity of the coaxial cable	2.1
Length of the coaxial cable	≈ 100 mm

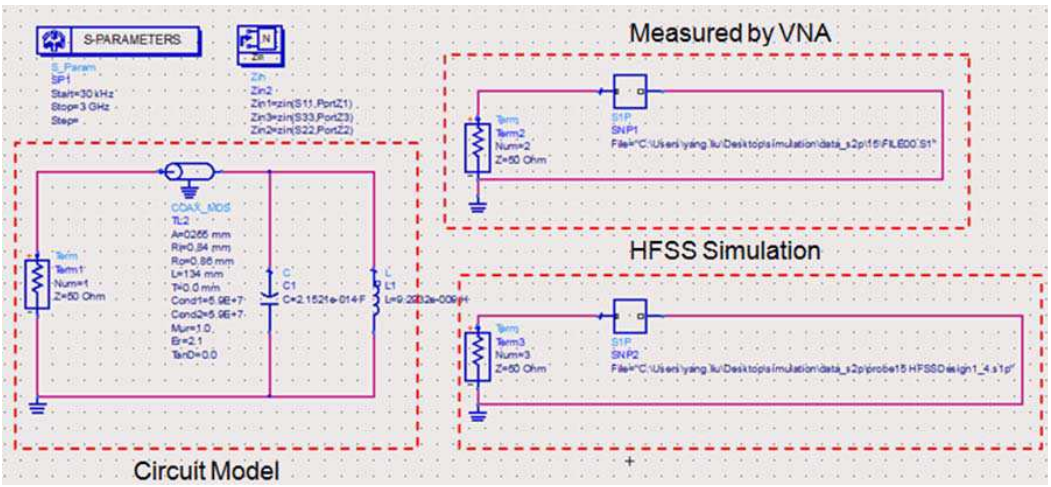

Figure 15. Circuit model simulation compared with the measurement and HFSS model implemented in the ADS schematic environment.

device. In this scope, we can identify the circuit model parameters by comparing the input impedance obtained with the circuit model simulation, the 3D EM simulation and also the measurement with a VNA. The ADS schematic environment provides a simple way to perform this comparison, and the only thing we need to do is to record the S-parameter extracted from HFSS and measured with the VNA, implemented for example, in touchstone format file.

Then, we imported these files into the ADS schematic environment to calculate the input impedance. The configuration of ADS simulation is featured in Fig. 15. We emphasize that the HFSS simulation and measurement results are thoroughly in good correlation from 30 kHz to 3 GHz. It is important to note that the circuit model can be improved by optimizing the calculated circuit parameters. By using the optimization function of ADS, more accurate circuit model of the magnetic probe was engendered. However, we can still exploit this model for the next step of the study by deeming with a model consisting of a microstrip transmission line as the DUT and the HFSS designed probe placed over the DUT which is excited by a transient signal with 1 V magnitude having frequency spectrum form DC to 300 MHz as plotted in the following figure. Then, the measured voltage $V_{mes}(t)$ is detected between the terminal ports of the probe. To verify the relevance of these calibration results, H-field at the center of the loop was recorded. This transient H-field component $H_y(t)$ is assumed as the total magnetic field though the loop. The calibration results are revealed in Fig. 16 which displays $H_y(t)$ obtained before and after calibration compared with CST simulation. This comparison states that the probe calibration with the circuit model visibly improves the measurement. The same H-field magnitude is found at the extreme points. One observes that the time delay due to the coaxial cable was also corrected. However, a slight difference was accentuated principally caused by the inaccuracies of the circuit model parameters.

With the 3D model of the measurement chain built with CST MWS depicted in Fig. 17, another

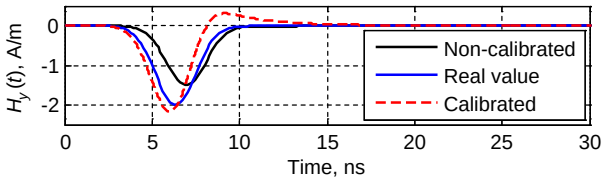

Figure 16. Comparison of $H_y(t)$ obtained with and without probe calibration.

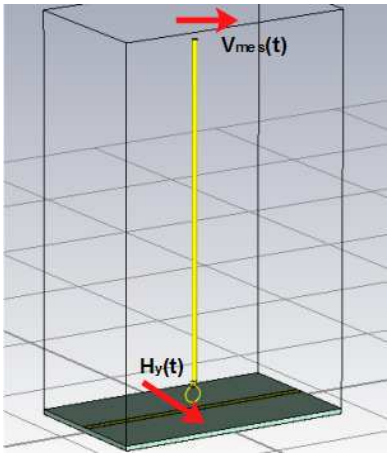

Figure 17. 3D model of the structure under investigation designed with CST MWS.

circuit model can also be assimilated to represent the design model schematized in Fig. 18(a). This circuit model takes into account the mutual inductance regarding the coupling between the probe and the DUT which is considered as a distributing circuit model. Then, by optimizing the circuit model's parameters and the coupling coefficient, an accurate circuit model can be accomplished. When the inductive coupling circuit model is built, one can use it as a black box that contains the two ports S-matrix. The input and output ports represent the DUT excitation and the voltage induced by the probe. By comparing with the CST simulation results, a simple example has been made. A good accordance between $H(t)$ can be encountered visibly in Fig. 18(b). Consequently, the circuit model calibration technique is established and verified by the measurement demonstration with the support of different simulation tools. The advantage of this calibration from the circuit model is to provide a simple method to deduce the induced voltage from the measured voltage, when certain components, as amplifier or connection cable, are changed or added into the measurement chain. In fact, the complementary elements can be expressed as S-matrix which can be easily plugged in the circuit model.

4.3. Calibration Technique Using a Reference Device

So far, the circuit model of the full measurement chain was implemented by way of simulation tools. On the other hand, we also manage to validate the probe calibration by considering a measurement reference device. Of course, a calibration structure with predefined magnetic NF values, for example based on the theoretical formulae, is required. A proof of concept consisting of transmission line was designed, fabricated and considered in order to calibrate the probe. More concretely, the reference device comprises a metal cable placed over a ground plane as sketched in the left of Fig. 19. The EM field can be calculated mathematically in the FD by changing the source as a time-dependent variable. By denoting $\eta = \sqrt{\mu_0/\varepsilon_0} = 120\pi$ the wave impedance, $d = \sqrt{h^2 - a^2}$, $K = V(t)/\ln((h+d)/(h-d))$ and $V(t)$ as the time-dependent voltage source, one can transpose these analytical formulae for the TD calculation, given as:

$$\begin{cases} E_y = 8Kyzd \Big/ \left[\left(y^2 + (z+d)^2\right)\left(y^2 + (z-d)^2\right)\right] \\ E_z = 4Kd\left(y^2 - z^2 + d^2\right) \Big/ \left[\left(y^2 + (z+d)^2\right)\left(y^2 + (z-d)^2\right)\right] \\ H_y = -E_z/\eta \\ H_z = E_y/\eta \end{cases} . \tag{7}$$

First, these analytical expressions were validated with CST MWS simulations by exciting the reference device with a sine voltage signal with 500 MHz frequency and $2V_{pp}$ amplitude. The comparison results are given in Figs. 20(a), (b), (c), (d) for $E_y(t)$, $E_z(t)$, $H_y(t)$ and $H_z(t)$, respectively. Comparisons

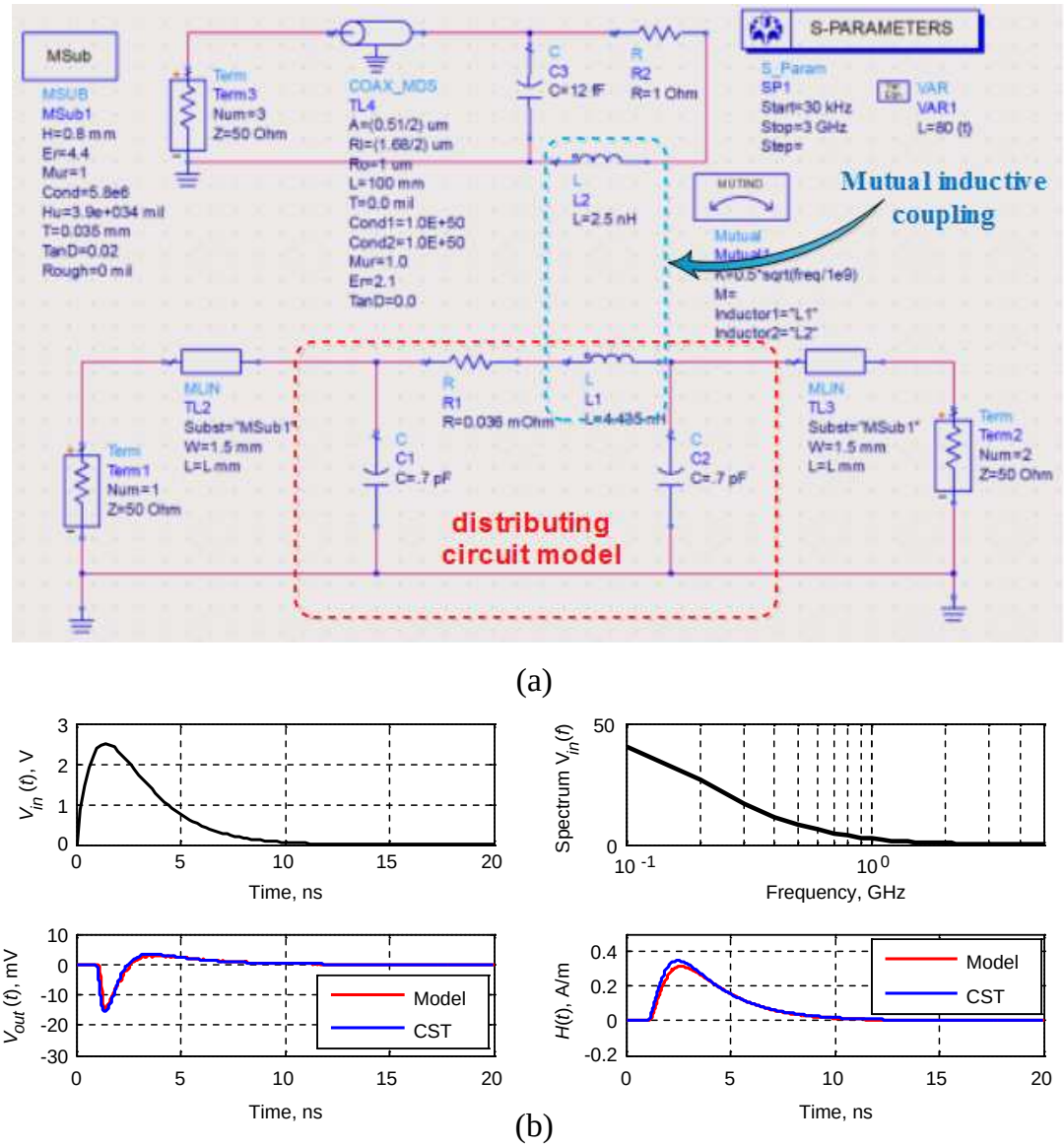

Figure 18. (a) Circuit model based on the mutual inductive coupling and distributing circuit model. (b) Comparison of the time-dependent results obtained with the mutual inductive coupling circuit model and CST simulation.

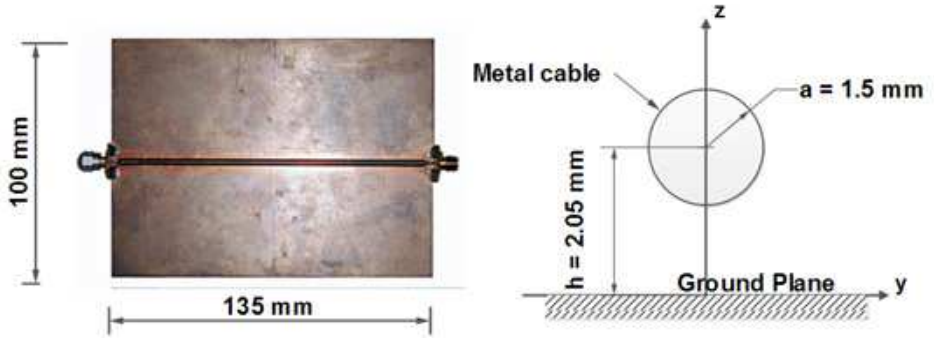

Figure 19. Calibration reference device constituted by a grounded cylindrical line.

of the EM NF profiles and the time variations are performed in these figures. We can see that good correlations were confirmed.

5. TD NF PLANAR SCAN METROLOGY WITH THE TEST BENCH DEVELOPED

This section is focused on the practicality study of the NF scan test bench described earlier in Fig. 4 with case of applications in order to validate the TD metrology. For that, TD scanning of RF planar passive circuits will be carried out.

5.1. Experimental Analysis of the Reference Device for the Magnetic TD NF Scan

A photograph of the considered experimental setup for characterizing the TD NF metrology understudy is displayed in Fig. 21. The model of the cable above the ground plane is assigned as the DUT. This structure is excited by a 20 MHz sine voltage signal with $20V_{pp}$ amplitude. Then, the induced voltage at different points above the DUT is recorded by the oscilloscope. Finally, we determined $H_y(t)$ from the analytical expression based on the measured voltage. To validate the TD NF test bench, comparisons

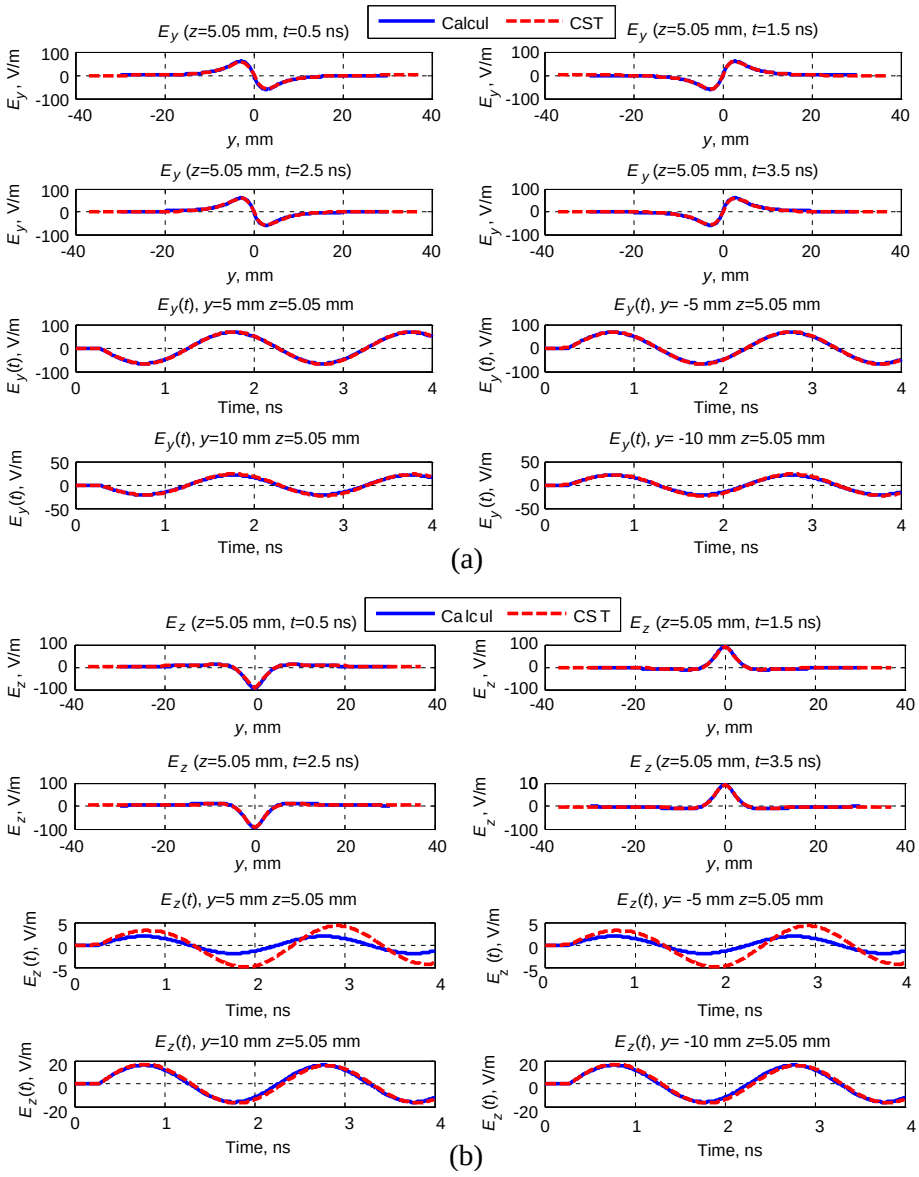

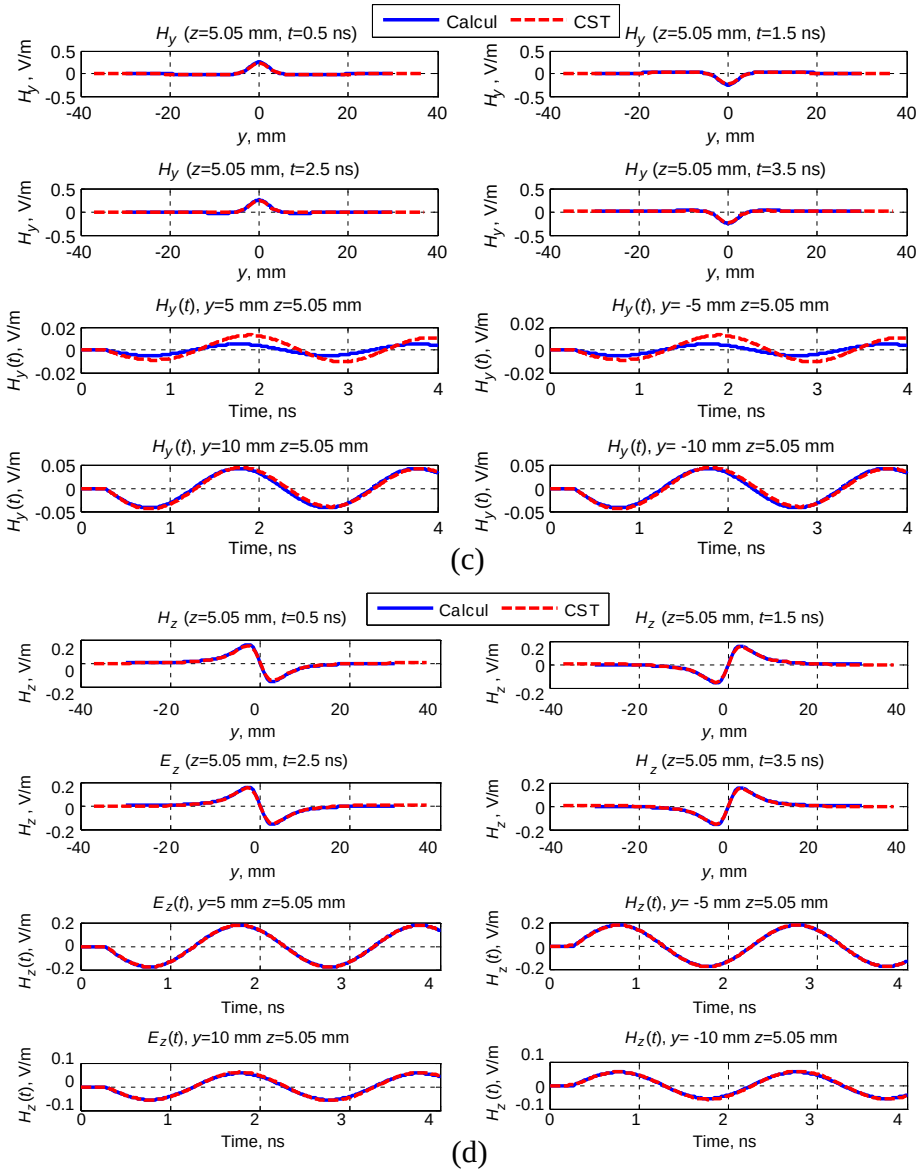

Figure 20. (a) Comparisons of $E_y(t)$ obtained by the analytical calculation and CST simulation. (b) Comparisons of $E_z(t)$ obtained by the analytical calculation and CST simulation. (c) Comparisons of $H_y(t)$ obtained by the analytical calculation and CST simulation. (d) Comparisons of $H_z(t)$ obtained by the analytical calculation and CST simulation.

of the magnetic field obtained from the analytical calculations and experimental measurements were completed.

According to these results, a good agreement between the amplitudes of $H_y(t)$ with measurement points at some mm in proximity of the cable is witnessed. The improbable imperfection is larger when the measurement points are situated far away from the cable. It is important to note that the time lag between calculated and measured $H_y(t)$ is due to the time reference point of the oscilloscope.

To check the limit of validation with this calibration probe model, further study is necessary. To do this, the magnetic field cartography with a typically complex wide band signal was surveyed. A simple example has been considered with the analytical calculation and CST simulation. The DUT is excited by a transient UWB signal, plotted in Fig. 22. Then, the cartographies of $H_y(t)$ presented in Fig. 23 are generated from analytical calculations and simulations. Through these comparisons, the area where

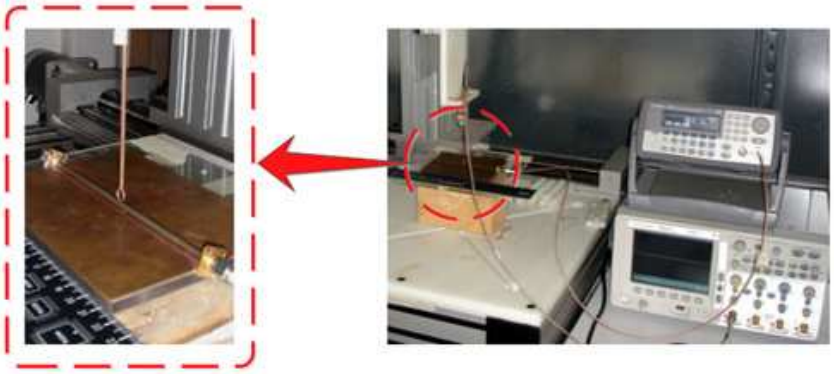

Figure 21. Experimental set up for the EM NF measurement in the TD.

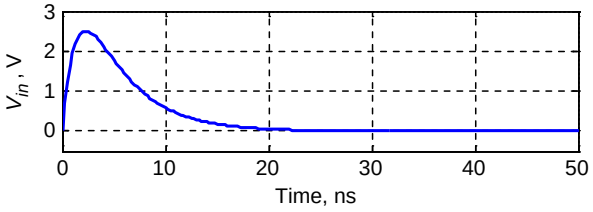

Figure 22. Transient excitation signal considered during the test.

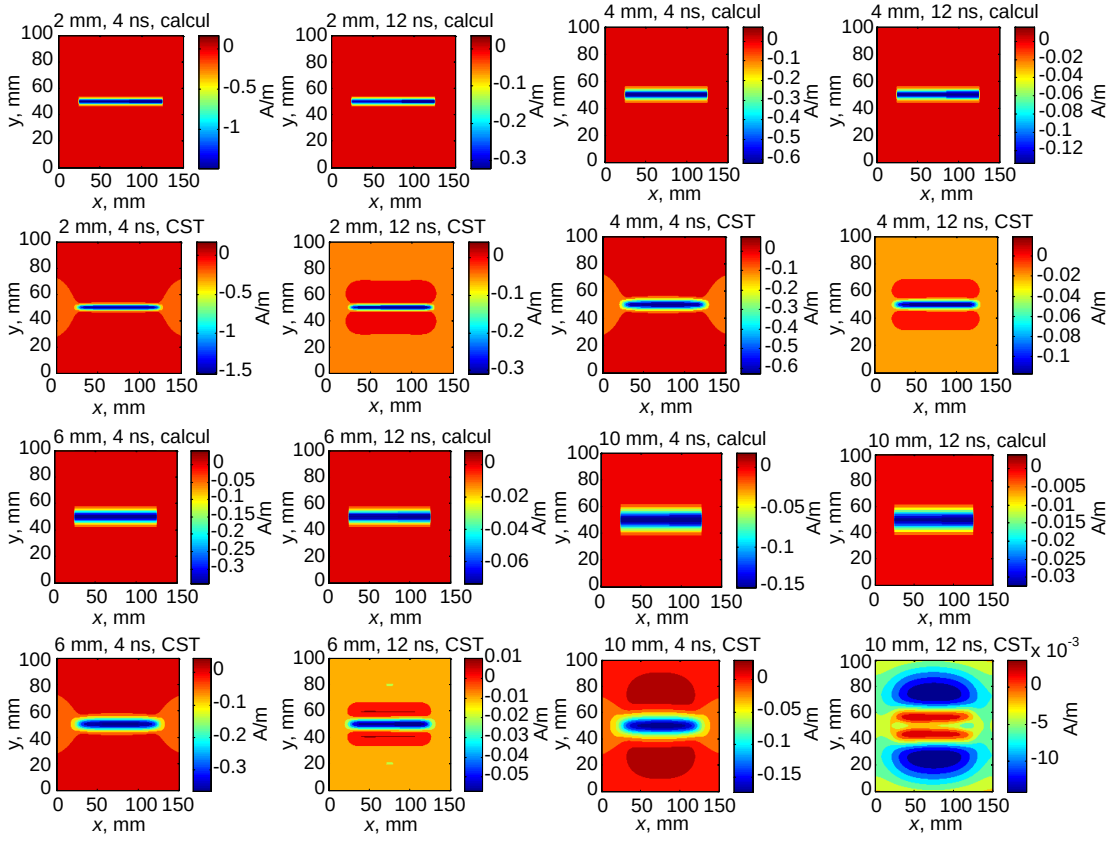

Figure 23. NF maps of $H_y(t)$ obtained from analytical calculations and simulations.

we can have the good correlation and where we cannot are worth noting. In general, the calibration technique with the cable and ground plane model was established by theoretical analyses, simulations and experimentations. However, further correction study should be conducted continuously to improve these results.

5.2. Measurement with UWB Amplifier

During the measurement with the TD NF bench, we accentuate that the presence of noise effect from the digital oscilloscope could perturb seriously the measurement results. On one hand, the range of the oscilloscope is about ±5 mV. When the induced voltage drops into this range, it cannot be detected and measured by the oscilloscope. On the other hand, the issue linked to the oscilloscope imperfection manifests a DC-offset of the voltage measured. Knowing the linearity of the probe transfer function, the presence of DC-offset could change the H-field waveform. For example, Fig. 24 illustrates the measurement perturbation by comparing the H-field deduced from the induced voltage with and without the biasing errors. To resolve this problem and avoid probable perturbations generated by the oscilloscope, we insert a super UWB amplifier between the probe and the oscilloscope in order to amplify the captured signal. For this purpose, a prototype of amplifier has been designed, fabricated and tested. Its layout design and photograph are displayed in Fig. 25. This amplifier is composed of a two-stage circuit based on the Operational Amplifier LMH6703.

Table 4. Parameters of the amplifier shown in Fig. 25.

VNA	Input power	Frequency range	Number of points	DC supply
HP 8753E	−40 dBm	40 MHz to 2 GHz	201	±5 V

The nominal voltage gain absolute value of the single stage amplifier with measurement parameters addressed in Table 4 is about A_{vdB}=20 dB. For our application, a two-stage amplifier cascaded is implemented to achieve the gain value large enough. After test, the total average gain of the two stage amplifier is measured, about 40 dB. This amplifier was tested by using the VNA HP8753E with the input power −40 dBm and the frequency band from 40 MHz to 2 GHz. Therefore, we found both the magnitude and the phase of the S-parameters varied with the frequency. As expected, the transmission parameter S_{21} is about 40 dB at low frequencies. However, it falls out to −17 dB at 2 GHz. This gives the −32 dB/decade gain slope. At the frequency of about 300 MHz, the gain is slightly above 30 dB. At 1 GHz, the experimented gain is equal to 11 dB. Please note that all these gains are evaluated with 50 Ω termination reference impedances. The phase delay is quite linear. We emphasize that the magnitude of reverse transmission parameter S_{12} of the amplifier is very low and better than −40 dB up to 900 MHz and average voltage gain of about 20 dB at the frequencies below 700 MHz. However, the gain is not flat enough and drops down with the −32 dB/decade rate. The gain at different frequencies is summed up in Table 5. In conclusion, the amplifier can be used to separate the captured signal from the noise for the measuring frequency lower than 1.4 GHz. The cartography of the TD NF will be carried out with the two-stage amplifier in the next section.

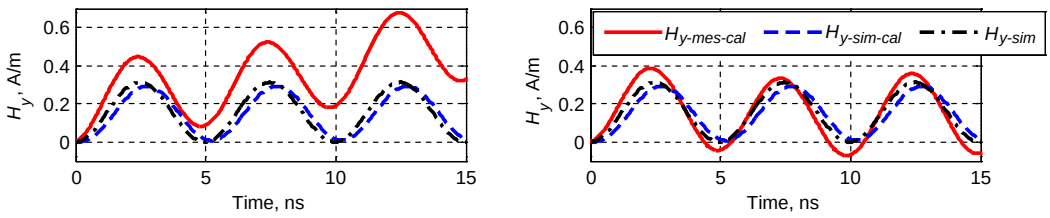

Figure 24. Illustration of biasing error induced by the digital oscilloscope to $H_{mes}(t)$.

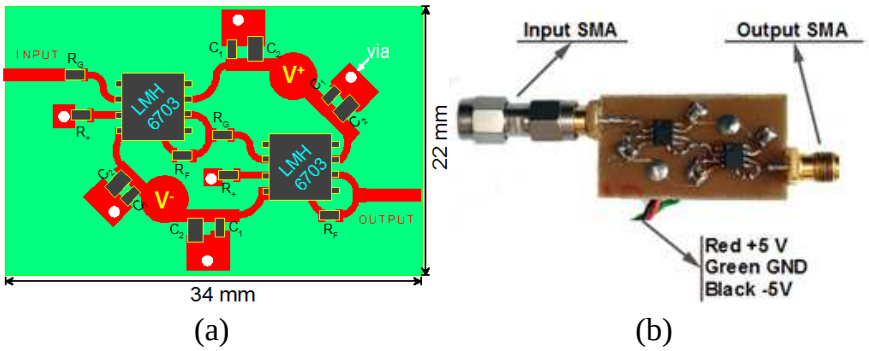

Figure 25. (a) PCB design and (b) constructed amplifier circuit.

Table 5. Measured gain of the amplifier shown in Fig. 25 versus frequency.

Frequency	300 MHz	400 MHz	500 MHz	600 MHz	700 MHz
Gain	31.1 dB	28.6 dB	26.3 dB	23.7 dB	21.0 dB

5.3. TD Scanning of Magnetic NF Radiated by RF Circuits

To state the relevance of this full TD NF scan, EM transient radiation of arbitrary concrete electronic planar RF devices was experimented and explored. The outcomes including the analysis of the TD metrology are outlined in the next paragraphs.

5.3.1. Description of the Microstrip Devices Understudy and the Considered Experimental Setup

To operate with RF/microwave transient signals, we perform measurements of a planar microstrip device which is commonly used in modern electronic systems. In practice, it acts as a Chebychev filter. During the test, a loop probe having 6 mm diameter is placed over the DUT to scan H_y at the 5 mm height. The DUT is excited by a square wave signal. The physical sizes of the DUT are monitored in this Fig. 26.

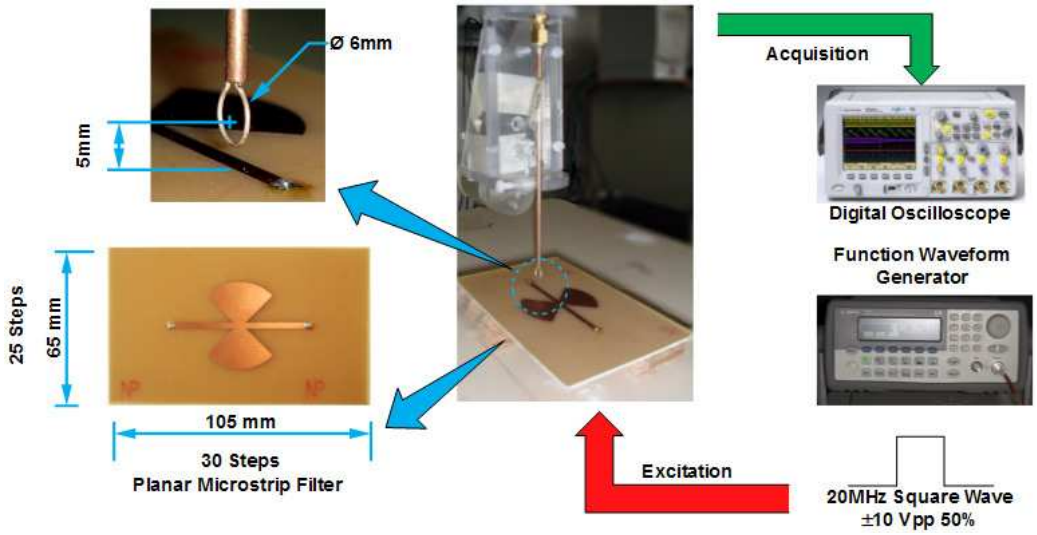

Figure 26. Experimental setup for the measurement of the magnetic NF emitted by a butterfly planar filter.

The spatial resolutions correspond to the scanning point number set to $N_x \times N_y = 30\,(x\text{-axis}) \times 25\,(y\text{-axis})$. For starting, the DUT was excited with 20 MHz square wave signal having $20V_{pp}$ amplitude and 50% duty cycle plotted in Fig. 27. Then, the voltage delivered by the probe is measured with the digital oscilloscope Agilent MSO6104. The time-dependent signal was recorded as 1000 sampling points. Due to the performance of PC and oscilloscope, the measurement is very time-consuming. For such a planar surface scan and step number, the field scanning costs more than four hours. After applying the transfer function, we achieve the magnetic NF cartography in the TD displayed in Fig. 28(a). In this figure, the influence of the connection cable and the time-dependent periodical variation of the field maps can be observed undeniably. To highlight the time-dependent magnetic field $H_y(t)$, we examine the results at different positions in the scanning plan stated in Fig. 28(b). As discussed before, we still can find small DC-offset in the figures. This is due to the biasing effects internally generated by the digital oscilloscope.

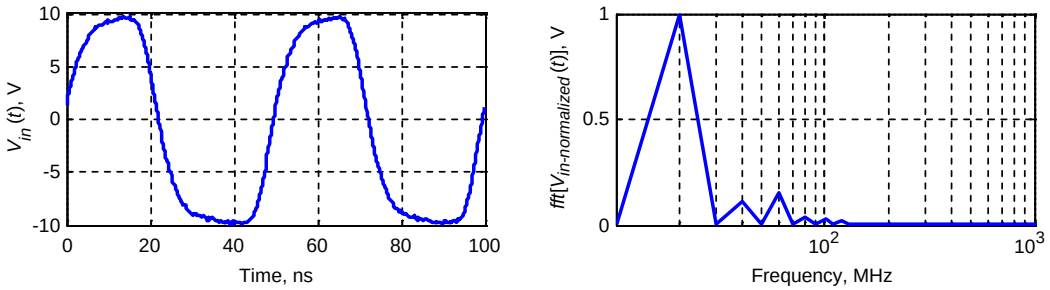

Figure 27. Excitation signal considered and its spectrum.

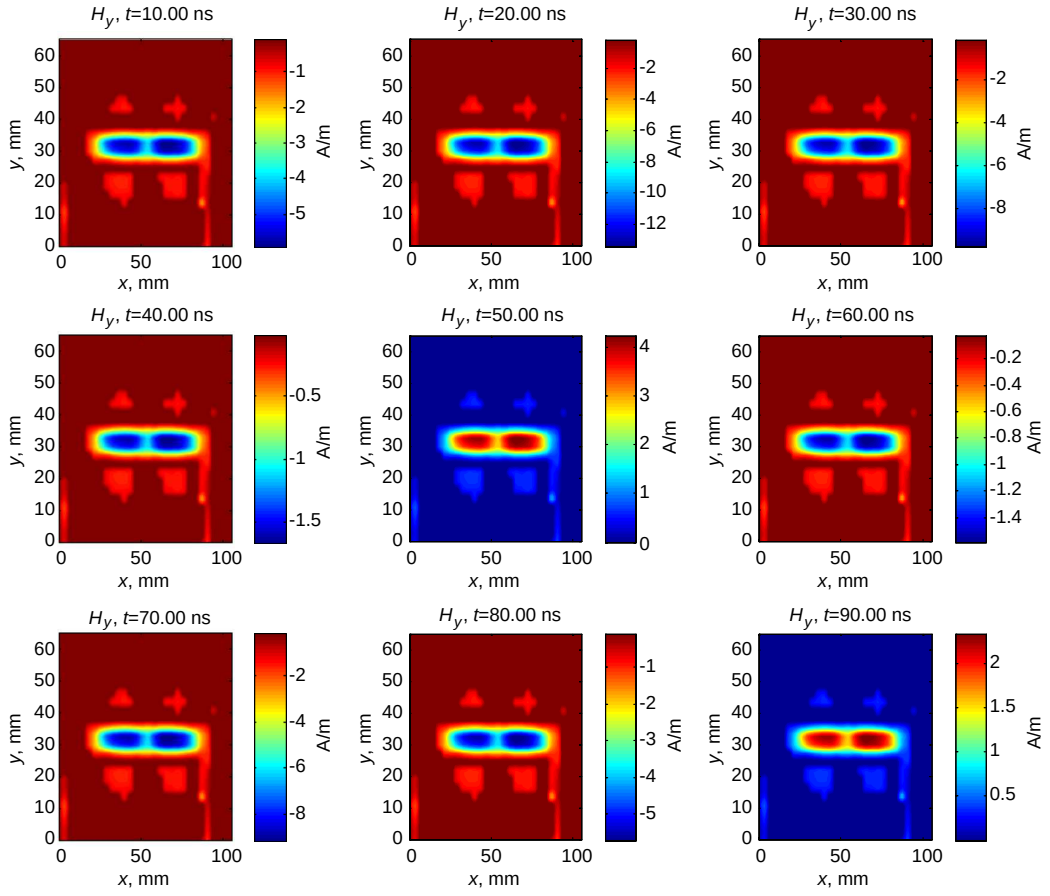

(a)

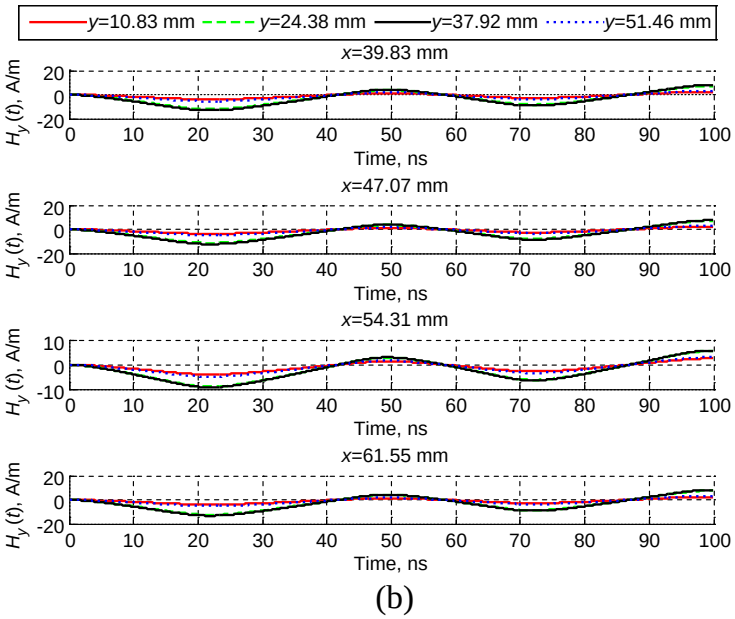

(b)

Figure 28. (a) Field maps at different time of $H_y(t)$ measured. (b) Time-dependent magnetic NF $H_y(t)$ at different positions.

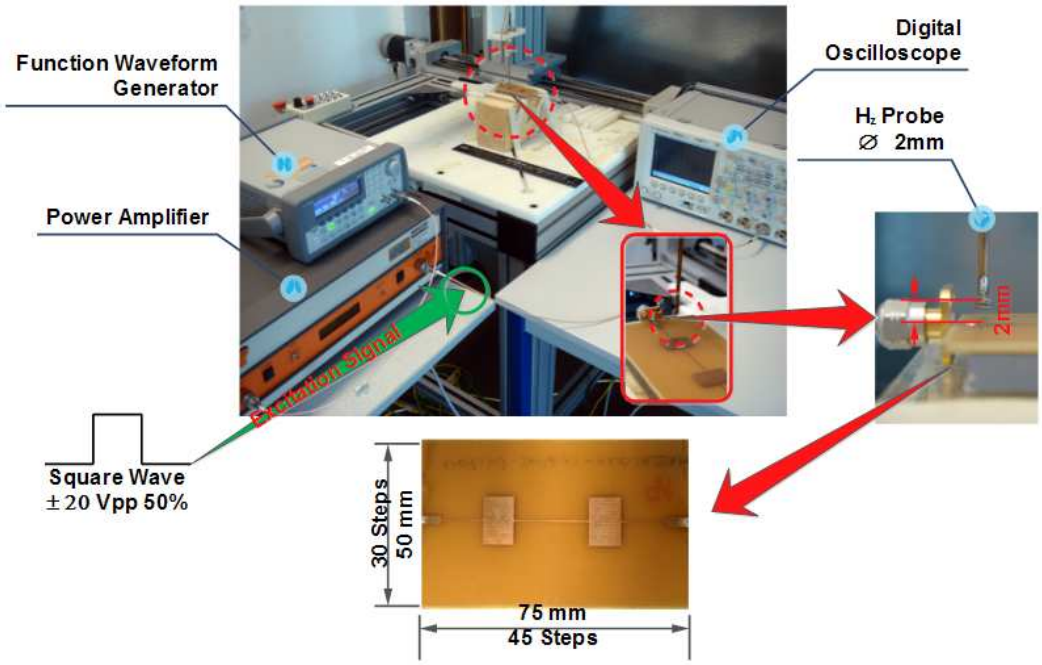

Figure 29. Measurement setup to map H_z radiated by the Chebychev filter.

However, the TD H-field mapping in a 2D plane is accomplished successfully with the test bench developed. Furthermore, another measurement demonstration is performed to uphold the relevance of the investigated NF measurement technique. This second series of experimental demonstration is dedicated to map $H_z(t)$ radiated by a planar microstrip Chebychev filter. The measurement setup is sketched in Fig. 29. To do this, z-component H-field probe consisted of two-turns loop with diameter of 2 mm was considered. It is placed at 2 mm above the metallic plane of the DUT having dimension 75 mm × 50 mm. This DUT was discretized with spatial sampling points $N_x \times N_y = 45 \times 30$. A power

amplifier was employed to amplify the excitation signal from the considered function generator. The amplified excitation voltage is plotted in Fig. 30. Then, the NF maps of $H_z(t)$ from the fully TD experimental setup introduced in Fig. 29 are viewed in Fig. 31(a) for t varying from 10 ns to 90 ns with step of 10 ns. Furthermore, the time-dependent maps of $H_z(t)$ detected at different positions are depicted in Fig. 31(b). Once again, the magnetic NF cartography was carried out successfully. In these field maps, the effect of excitation ports cannot be ignored.

By comparing the time-varying results of the two measurements, it should be pointed out that the use of high-level signal enables to effectively avoid the DC-offset biasing effect. It is proved that the utilization of both a powerful input signal and a UWB amplifier is particularly efficient to resolve

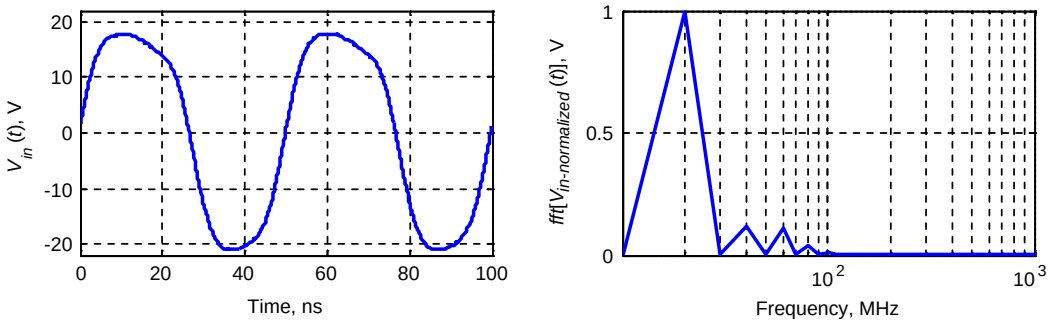

Figure 30. Excitation signals considered to excite the Chebychev filter shown in Fig. 29.

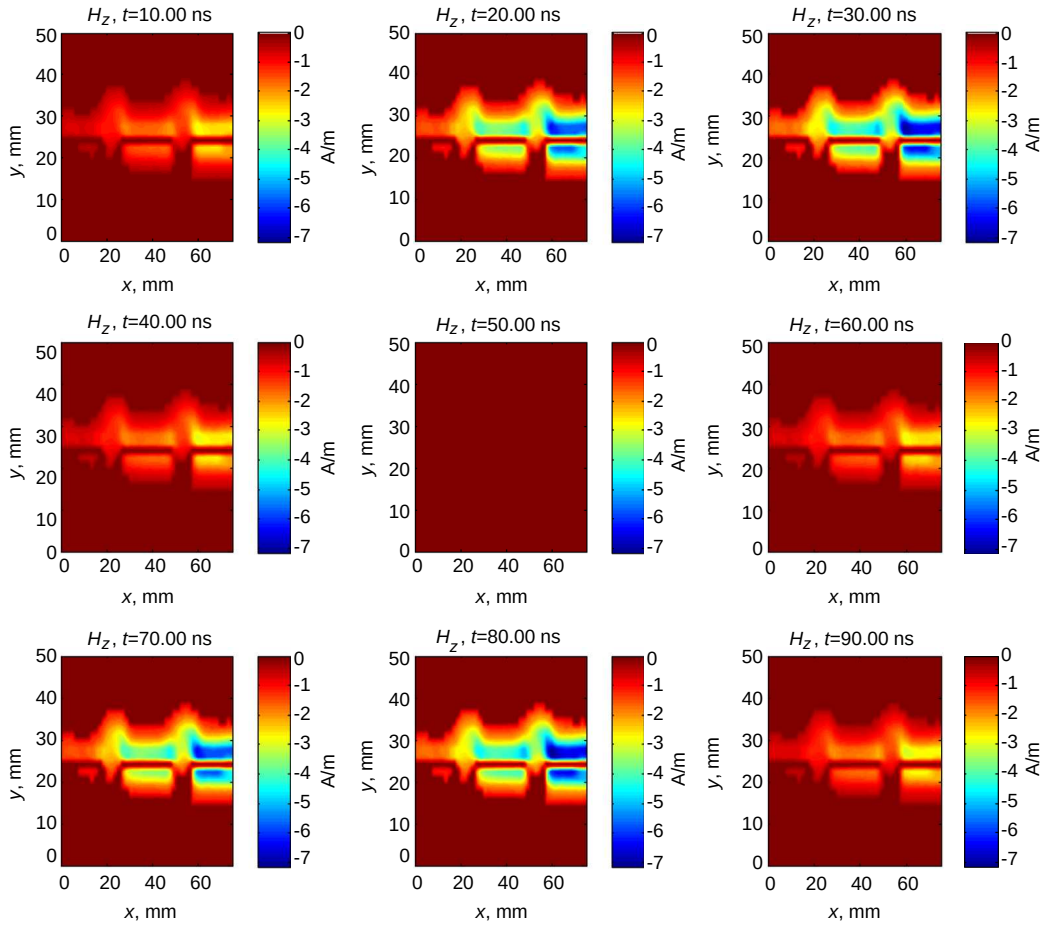

(a)

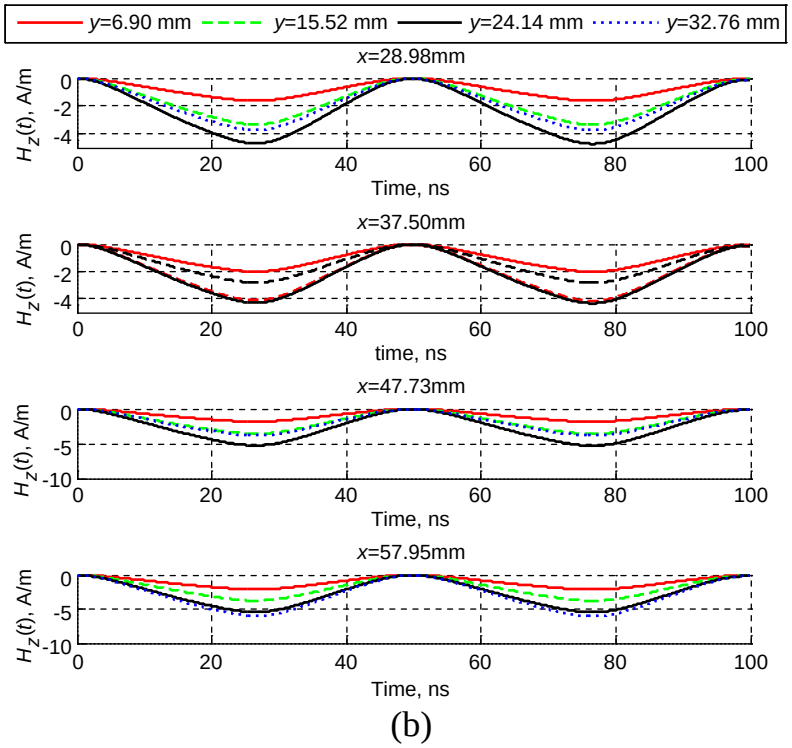

Figure 31. (a) Field maps of the measured $H_z(t)$ radiated by the DUT shown in Fig. 29. (b) Time-varying H-field value $H_z(t)$ at different positions.

this experimental imperfection. So far, we investigate the EM NF scanning fully in TD by considering planar passive circuits by using the developed measurement techniques. We emphasize that the quality of the results depends mainly on the calibration technique of the probe under consideration and also the performance of the oscilloscope. It is worth noting that in this case, the reference signal was assimilated as the excitation signal.

We emphasize that comparison between TD near-field computation results from broadband frequency measurements and full wave 3D EM simulations run with CST [44] applied to the same DUT was forwarded in [30, 58]. It was pointed out that the obtained time-domain NF data proposed can also be validated with full wave computation results or by frequency data convoluted with the transient excitation by means of FFT.

6. CONCLUSION

A full TD EM NF scanning technique was investigated. The measurement technique is based on the use of electronic probes implemented in the IRSEEM NF test bench which was initially employed in the FD.

Thanks to the examination of the probe transfer function, we transpose successfully this direct scanning technique into the TD. Then, the TD calibration of the measurement chain including the probe, cable and all the test equipment has been established and analyzed by means of different powerful circuit and full wave simulation tools (ADS, HFSS, CST MWS). In order to validate the TD NF metrology understudy, we also developed analytical formulae enabling to extract the magnetic NF radiation and cartographies in the TD. The considered model is also used to calibrate the measurement chain in the FD. In order to increase the level of the measured signals and minimize the unwanted noise effect combined with the biasing issue, an UWB amplifier was designed and fabricated then, inserted in the measurement chain. As expected, significant levels of the transient voltages corresponding to the magnetic NF radiated by the DUT were recorded. However, the amplifier's design still needs to be

optimized according to the frequency band of the transient perturbations, for example, met in different areas of EMC applications.

To automatize the test bench with the 2D plane sweeping operation, a graphical software interface was emulated and implemented in the chain of TD NF test bench in order to synchronize the probe displacement and the data acquisition. The interface and algorithmic process emulated in graphical language LabVIEW provided by NI^{TM}. An executable application program named as TDNF was developed. Afterward, to check the relevance of the measurement process, several planar electronic devices were experimented. As expected, in the scope of radiating EMC analyses, planar maps of magnetic fields situated at some mm above the metallic planes of the DUT were reconstructed and validated successfully.

As an ongoing research, to improve the proposed TD NF test bench, further work summarized in the following points is currently in progress:

- We are currently developing a basic algorithm to improve the interface processing and data acquisition including the correction process of probable measurement errors. New function will be considered such as manual control associated with results display.
- A measurement method of EM NF radiation emitted by complex autonomous circuits in the TD is planned. For this purpose, we consider to characterize the EM NF radiation emitted by a simple active circuit. To do this, as preliminary study and a future step of this work, a chopper circuit is chosen as the DUT which is widely used in the power electronic area. Even, the creation of the signal synchronization reference when considering complex mixed circuits as mother boards should be taken into account for further amelioration, in order to achieve the more accurate results containing the time lag for different positions.
- To achieve more accurate data and higher resolution, the measurement equipment especially the probe technology needs to be enhanced. As solution, one of key elements is the design and realization of electronic miniaturized probes with high sensitivity. Facing to this technical bottleneck, different innovative solutions were already proposed. More concretely, ADS designs of NF scanning electric and magnetic active probes with amplifier integrated were carried out and currently under fabrication. Three packs of implementation were already executed first, the realization in multilayer, MMIC and CMOS technologies.
- Finally, as argued previously, in the scope of the TD EMC applications, to measure typically ultra-high speed transient emissions, improved technique with very high performance oscilloscope with bandwidth more than 20 GSa/s is planned to achieve a good quality of NF scanning data.

ACKNOWLEDGMENT

Acknowledgement is made to European Union and Upper Normandy region in FRANCE for the support of this research through the INTERREG IVA France-Channel-UK and FEDER European Programme by funding project No. 4081 entitled "Time-Domain Electromagnetic Characterization and Simulation for EMC applications (TECS)".

REFERENCES

1. Baum, C. E., "Emerging technology for transient and broad-band analysis and synthesis of antennas and scatterers," *Proc. of IEEE*, Vol. 64, No. 11, 1598–1616, Nov. 1976.
2. Jauregui, R., M. Pous, M. Fernández, and F. Silva, "Transient perturbation analysis in digital radio," *Proc. of IEEE International Symposium on Electromagnetic Compatibility (EMC 2010)*, 263–268, Fort Lauderdale, FL, USA, Jul. 25–30, 2010.
3. Schuster, J., R. Luebbers, and H. Riazi, "FDTD predictions and measurements of car effects on portable telephone received signal levels," *1996 (AP-S) Digest IEEE Antennas and Propagation Society International Symposium*, Vol. 1, 426–428, Baltimore, MD, USA, Jul. 21–26, 1996.
4. Kasuga, T., M. Tanaka, T. Komakine, and H. Inoue, "Estimation of spatial distribution of electromagnetic noise radiated from PCB," *Proc. of IEEE International Symposium on*

Electromagnetic Compatibility (EMC 2010), Vol. 1, 369–374, Washington, DC, USA, Aug. 21–25, 2000.

5. Montrose, M. I., *Printed Circuit Board Design Techniques for EMC Compliance: A Handbook for Designers,* 2nd Edition, Wiley-IEEE Press, New York, USA, Jun. 2000.
6. Archambeault, B. R., C. Brench, and S. Connor, "Review of printed-circuit-board level EMI/EMC issues and tools," *IEEE Tran. EMC*, Vol. 52, No. 2, 455–461, May 2010.
7. Schoenmaker, W. and P. Meuris, "Evaluation of the electromagnetic coupling between microelectronic device structures using computational electrodynamics," *Proc. of 7th International Conference on Scientific Computing in Electrical Engineering (SCEE 2008)*, 61–65, Helsinki University of Technology, Espoo, Finland, Sep. 28–Oct. 3, 2008.
8. Youssef, M., J. Roudet, and Y. Marechal, "Near-field characterisation of power electronics circuits for radiation prediction," *Proc. of 28th Annual IEEE Power Electronics Specialists Conference, (PESC' 97)*, Vol. 2, 1529–1534, St. Louis, MO, USA, Jun. 22–27, 1997.
9. Frank, F. and R. Weigel, "An efficient neural network based modeling method for automotive EMC simulation," *Frequenz*, Vol. 65, Nos. 9–10, 267–271, Sep. 2011.
10. Mainville, S., "Automotive EMC case study: HMI graphics influence on radiated emissions," *Proc. of IEEE International Symposium on Electromagnetic Compatibility (EMC 2010)*, 620–624, Fort Lauderdale, FL, USA, Jul. 25–30, 2010.
11. Egot, S., M. Klingler, L. Kone, S. Baranowski, and B. Demoulin, "Influence of the PCB traces of an automotive electronic equipment in the case of random cable harnesses," *Proc. of 16th International Zurich Symposium on EMC*, 125–130, Zurich, Switzerland, Feb. 13–18, 2005.
12. Pelton, E., W. Burnside, and N. Wang, "Analysis for predicting near-field effects of on-aircraft antennas," *1978 Antennas and Propagation Society International Symposium*, Vol. 16, 81–84, University of Maryland, New York, USA, Mar. 15–19, 1978.
13. Sarma, A. D. and N. S. Murthy Sarma, "Near field radiation pattern analysis of on-aircraft antennas using UTD," *Proc. of International Conference on Electromagnetic Interference and Compatibility'97*, 167–170, Hyderabad, India, Dec. 3–5, 1997.
14. Gray, R. I., "Near field coupling to aircraft in the 1–30 MHz band," *Proc. of 1968 IEEE Electromagnetic Compatibility Symposium Record*, Vol. 10G, 253–261, Seattle, WA, USA, Jul. 23–25, 1968.
15. Winter, W. and M. Herbrig, "Time domain measurements in automotive applications," *Proc. of IEEE International Symposium on Electromagnetic Compatibility, (EMC 2009)*, 109–115, Austin, Texas, USA, Aug. 17–21, 2009.
16. Lawton, S., D. D. Ward, S. R. Cloude, and J. F. Dawson, "Hybrid time domain modelling for automotive EMC," *Proc. of 2nd International Conference on Computation in Electromagnetics*, 275–278, London, UK, Apr. 12–14, 1994.
17. Shi, J., M. A. Cracraft, J. Zhang, R. E. DuBroff, K. Slattery, and M. Yamaguchi, "Using near-field scanning to predict radiated fields," *Proc. of IEEE International Symposium on Electromagnetic Compatibility, (EMC 2004)*, Vol. 1, 14–18, Santa Clara, USA, Aug. 9–13, 2004.
18. De Daran, F., F. Lafon, and D. Allou, "Near field μC model for PCB radiated field prediction," *Proc. of 2nd Int. Conference on Electromagnetic Near-field Characterization and Imaging (ICONIC)*, Barcelona, Spain, Jun. 8–10, 2005.
19. Boyer, A., E. Sicard, and J. L. Levant, "On the prediction of near-field microcontroller emission," *Proc. of International Symposium on Electromagnetic Compatibility, (EMC 2005)*, Vol. 3, 695–699, Chicago, Illinois, USA, Aug. 8–12, 2005.
20. Serhir, M., P. Besnier, and M. Drissi, "An accurate equivalent behavioural model of antenna radiation using a mode-matching technique based on spherical near field measurements," *IEEE Tran. Ant. Prop.*, Vol. 56, No. 1, 48–57, Jan. 2008.
21. Barriere, P.-A., J.-J. Laurin, and Y. Goussard, "Mapping of equivalent currents on high-speed digital printed circuit boards based on near-field measurements," *IEEE Tran. EMC*, Vol. 51, No. 3, 649–658, Aug. 2009.

22. Vives, Y., C. Arcambal, A. Louis, F. de Daran, P. Eudeline, and B. Mazari, "Modeling magnetic radiations of electronic circuits using near-field scanning method," *IEEE Tran. EMC*, Vol. 49, No. 2, 391–400, May 2007.
23. Vives-Gilabert, Y., C. Arcambal, A. Louis, P. Eudeline, and B. Mazari, "Modeling magnetic emissions combining image processing and an optimization algorithm," *IEEE Tran. EMC*, Vol. 51, No. 4, 909–918, Nov. 2009.
24. Gilabert, Y. V., C. Arcambal, D. Baudry, A. Louis, B. Mazari, S. Alves, M. Stanislawiak, and P. Eudeline, "Modeling radiation sources of electronic components," *Proc. of IEEE International Symposium on Electromagnetic Compatibility, (EMC 2006)*, Vol. 1, 89–92, Portland, OR, USA, Aug. 14–18, 2006.
25. Tong, X., D. W. P. Thomas, K. Biwojno, A. Nothofer, P. Sewell, and C. Christopoulos, "Modeling electromagnetic emissions from PCBs in free space using equivalent dipoles," *Proc. of European Microwave Conference, (EuMC 2009)*, 280–283, Rome, Italy, Sep. 29–Oct. 1, 2009.
26. Cicchetti, R., "Transient analysis of radiated field from electric dipoles and microstrip lines," *IEEE Tran. Ant. Prop.*, Vol. 39, No. 7, 910–918, Jul. 1991.
27. Hansen, T. B. and A. D. Yaghjian, "Planar near-field scanning in the time domain, Part 1: Formulation," *IEEE Tran. Ant. Prop.*, Vol. 42, No. 9, 1280–1291, Sep. 1994.
28. Hansen, T. B. and A. D. Yaghjian, "Planar near-field scanning in the time domain, Part 2: Sampling theorems and computation schemes," *IEEE Tran. Ant. Prop.*, Vol. 42, No. 9, 1280–1291, Sep. 1994.
29. Quan, S., "Time domain analysis of the near-field radiation of shaped electrically large apertures," *IEEE Trans. Ant. Prop.*, Vol. 58, No. 2, 300–306, Feb. 2010.
30. Ravelo, B. and Y. Liu, "Computation of transient near-field radiated by electronic devices from frequency data," *Fourier Transform Applications, InTech Open Science Book*, Chapter 1, 3–26, M. Salih, Ed., Apr. 2012.
31. Liu, Y. and B. Ravelo, "Application of near-field emission processing for microwave circuits under ultra-short duration perturbations," *Advanced Electromagnetics (AEM)*, Vol. 1, No. 3, 24–40, Oct. 2012.
32. Ravelo, B., Y. Liu, A. Louis, and A. K. Jastrzebski, "Study of high-frequency electromagnetic transients radiated by electric dipoles in near-field," *IET Microwaves Antennas & Propagation (MAP)*, Vol. 5, No. 6, 692–698, Apr. 2011.
33. Ravelo, B., "E-field extraction from H-near-field in time-domain by using PWS method," *Progress In Electromagnetics Research B*, Vol. 25, 171–189, 2010.
34. Ravelo, B., Y. Liu, and J. B. H. Slama, "Time-domain planar near-field/near-field transform with PWS operations," *Eur. Phys. J. Appl. Phys. (EPJAP)*, Vol. 53, No. 03, 1–8, Feb. 2011.
35. Lomné, V., P. Maurine, L. Torres, T. Ordas, M. Lissart, and J. Toublanc, "Modeling time domain magnetic emissions of ICs," *Integrated Circuit and System Design. Power and Timing Modeling, Optimization, and Simulation Lecture Notes in Computer Science*, Vol. 6448, 238–249, 2011.
36. Raiton, C. J., K. M. Richardson, J. P. McGeehan, and K. F. Elder, "Modelling electromagnetic radiation from digital electronic systems by means of the finite difference time domain method," *Proc. of Symposium Record, IEEE 1992 International Symposium on Electromagnetic Compatibility*, 38–43, Anaheim, California, USA, Aug. 17–21, 1992.
37. Lee, J.-F., R. Lee, and A. Cangellaris, "Time-domain finite-element methods," *IEEE Trans. Ant. Prop.*, Vol. 45, No. 3, 430–442, Mar. 1997.
38. Jiao, D., M. Lu, E. Michielssen, and J. Jin, "A fast time-domain finite element-boundary integral method for electromagnetic analysis," *IEEE Trans. Ant. Prop.*, Vol. 49, No. 10, 1453–1461, Oct. 2001.
39. Edwards, R. S., A. C. Marvin, and S. J. Porter, "Uncertainty analyses in the finite-difference time-domain method," *IEEE Trans. EMC*, Vol. 52, No. 1, 155–163, Feb. 2010.
40. Liu, L., X. Cui, and L. Qi, "Simulation of electromagnetic transients of the bus BAR in substation by the time-domain finite-element method," *IEEE Trans. EMC*, Vol. 51, No. 4, 1017–1025, Nov. 2009.

41. Jauregui, R., P. I. Riu, and F. Silva, "Transient FDTD simulation validation," *Proc. of IEEE International Symposium on Electromagnetic Compatibility, (EMC 2010)*, 257–262, Fort Lauderdale, Florida, USA, Jul. 25–30, 2010.
42. "EMPro 3D EM simulation software," Agilent 2000–2013, Online Available: http://www.home.agilent.com/en/pc-1297143/empro-3d-em-simulation-software.
43. "Electromagnetics, circuit & systems solutions," 2013 ANSYS Inc., Online Available: http://www.ansys.com/Products/Simulation+Technology/Electromagnetics.
44. "CST studio suite," 2013 CST Computer Simulation Technology AG, Online Available: http://www.cst.com/Content/Products/CST_S2/Overview.aspx.
45. "EMC Studio," 2012 EMCoS Ltd., Online Available: http://www.emcos.com/EMC.
46. Quickwave-3D, http://www.qwed.eu/qw_3d.html.
47. "Advanced EMC solutions — FEKO applications — EMC analysis," 2000 Advanced EMC Solutions, Inc. Online Available: http://www.aemcs.com/feko_applications_emc_analysis.html.
48. Baudry, D., C. Arcambal, A. Louis, B. Mazari, and P. Eudeline, "Applications of the near-field techniques in EMC investigations," *IEEE Tran. EMC*, Vol. 49, No. 3, 485–493, Aug. 2007.
49. Baudry, D., A. Louis, and B. Mazari, "Characterization of the open ended coaxial probe used for near field measurements in EMC applications," *Progress In Electromagnetics Research*, Vol. 60, 311–333, 2006.
50. Baudry, D., L. Bouchelouk, A. Louis, and B. Mazari, "Near-field test bench for complete characterization of components radiated emission," *Proc. of 4th International Workshop on Electromagnetic Compatibility of Integrated Circuits (EMC COMPO' 04)*, 85–89, Angers, France, Mar. 31–Apr. 1, 2004.
51. Manjombe, Y. T., Y. Azzouz, D. Baudry, B. Ravelo, and M. E. H. Benbouzid, "Experimental investigation on the power electronic transistor parameters influence to the near-field radiation for the EMC applications," *Progress In Electromagnetics Research M*, Vol. 21, 189–209, 2011.
52. Takahashi, M., K. Kawasaki, H. Ohba, T. Ikenaga, H. Ota, T. Orikasa, N. Adachi, K. Ishiyama, and K. I. Arai, "Optical scanning probe system for electromagnetic near field measurements," *Proc. of IEEE International Symposium on Electromagnetic Compatibility, (EMC 2009)*, 6–11, Austin, Texas, USA, Aug. 17–21, 2009.
53. Verdaguer, S., A. Vidal, A. Atienza, and F. Silva, "Time-domain measurement system for impulse noise characterization in digital communication environments," *Proc. of EMC Europe Workshop 2005, Electromagnetic Compatibility of Wireless Systems*, 73–76, Rome, Italy, Sep. 19–21, 2005.
54. Ordas, T., M. Lisart, E. Sicard, P. Maurine, and L. Torres, "Near-field mapping system to scan in time domain the magnetic emissions of integrated circuits," *Integrated Circuit and System Design. Power and Timing Modeling, Optimization and Simulation, Lecture Notes in Computer Science*, Vol. 5349, 229–236, 2009.
55. Shen, X.-J., X. Chen, Y. Zou, and Y. Zhang, "Time-domain planar near-field measurement simulation for wideband RCS and antenna," *Proc. of 2007 IEEE Radar Conference*, 535–540, Boston, MA, USA, Apr. 17–20, 2007.
56. Rioult, J., D. Seetharamdoo, and M. Heddebaut, "Novel electromagnetic field measuring instrument with real-time visualization," *Proc. of IEEE International Symposium on Electromagnetic Compatibility, (EMC 2009)*, 133–138, Austin, Texas, USA, Aug. 17–21, 2009.
57. Braun, S., C. Hoffmann, A. Frech, and P. Russer, "A real time time-domain EMI measurement system for measurements above 1 GHz," *Proc. of IEEE International Symposium on Electromagnetic Compatibility, (EMC 2009)*, 143–146, Austin, Texas, USA, Aug. 17–21, 2009.
58. Liu, Y., "Study of electronic circuit radiated near-field emissions in time-domain," Ph.D. Thesis Report, IRSEEM/ESIGELEC, University of Rouen, France, Oct. 2012.
59. Smith, G. S., "Antennas," *Antenna Engineering Handbook Loop,* 4th edition, J. Volakis (ed.), Chapter 5, McGraw-Hill, USA, 2007.